RSC Sustainability

ROYAL SOCIETY OF CHEMISTRY

PAPER

View Article Online
View Journal | View Issue

Cite this: *RSC Sustainability*, 2025, **3**, 5333

Cross-linked carboxymethyl cellulose–polyacrylic acid as a binder for thermally treated silicon–graphite@graphite based anodes: a multipronged approach towards realising silicon–graphite based anodes for lithium-ion cells

Aiswarya Samridh,[ac] Sumol V. Gopinadh,[b] Bibin John,*[b] Peddinti V. R. L. Phanindra,[b] J. Mary Gladis,*[c] S. Sujatha[b] and T. D. Mercy[b]

Received 13th March 2025
Accepted 8th September 2025

DOI: 10.1039/d5su00186b

rsc.li/rscsus

Silicon–graphite (Si–Gr) composites are widely studied as a commercially feasible alternative to pure silicon (Si) anodes in lithium-ion (Li-ion) cells, as they enable effective utilization of silicon's high energy density while mitigating performance degradation associated with volume expansion during cycling. The present study adopts a multipronged approach to tackle the volume expansion by (1) employing a crosslinked carboxymethyl cellulose–polyacrylic acid (CMC–PAA) binder, (2) supporting the Si–Gr composite in a graphite (Gr) matrix, Si–Gr@Gr, and (3) thermal treatment of the active material. While the CMC–PAA binder helps form a three-dimensional matrix embedding the Si–Gr@Gr active material, the graphite support acts as an additional buffer for the Si–Gr composite material by alleviating the mechanical stress during expansion. The thermal treatment of Si–Gr@Gr leads to oxide formation and modification of particle morphology and *d*-spacing, thereby facilitating easy movement of Li-ions and particle integrity. The anode processed *via* this approach exhibited an initial specific capacity of 940 mA h g^{-1} at a C/10 rate with a coulombic efficiency of 80.3% and demonstrated a specific capacity of 730 mA h g^{-1} after 1000 charge–discharge cycles with 78% capacity retention.

Sustainability spotlight

The use of fluorinated non-aqueous binders in electrode processing of lithium-ion battery manufacturing poses significant environmental and fiscal concerns. This study resolves this challenge by adopting aqueous binder-based anode processing for lithium-ion batteries. This also provides a promising path for reducing the carbon footprint of overall cell production. By using water as the solvent for electrode processing, the environmental and occupational hazards due to the conventional *N*-methylpyrrolidone (NMP) solvent can be eliminated. Also, the use of water as solvent lowers drying temperatures for electrodes offering a cost-effective alternative. Moreover, replacing the conventional fluorinated binder enhances the sustainability of batteries as it alleviates the challenges in disposal associated with the former.

1. Introduction

Silicon (Si), with its unmatched specific capacity of 3950 mA h g^{-1}, is a promising next generation anode material for improving the energy density of Li-ion batteries. Upon electrochemical lithiation, Si forms an amorphous Li_xSi alloy, the formation of which is associated with ~300% volume expansion. This leads to cracking of the electrode matrix, loss of adhesion to the substrate, loss of electrical conductivity, an increase in irreversible capacity fade due to repeated Solid Electrolyte Interphase (SEI) film formation, *etc.* Several strategies have been explored to mitigate the volume expansion of Si anodes, including the development of Si–Gr composite anodes, where graphite helps alleviate stress; the use of elastic binders that preserve electrode integrity; and the incorporation of conductive components to maintain electrical connectivity during cycling.[1] Mixing/compositing silicon with carbon (Si/C) is set to be a realistic strategy to overcome issues related to the volume changes of Si and the low capacity of graphite.[2]

Polyvinylidene fluoride (PVDF), the conventional non-aqueous binder, is reportedly proven to be incapable of sustaining the mechanical stresses developed in Si-based anodes as it is attached to Si particles *via* weak van der Waals forces only.[3] The paradigm shift towards sustainable electrode

[a]*Human Rating Certification Group, Vikram Sarabhai Space Centre, Thiruvananthapuram, India*

[b]*Energy Systems Group, Vikram Sarabhai Space Centre, Thiruvananthapuram, India. E-mail: bibin_john@vssc.gov.in*

[c]*Department of Chemistry, Indian Institute of Space Science and Technology, Thiruvananthapuram, India. E-mail: marygladis@iist.ac.in*

fabrication techniques underscores the importance of water-soluble binders with tailored properties. In addition to linear-chain binders, several other types have been reported, including branched-chain binders, crosslinked binders, conjugated conductive polymer binders, and binders containing active functional groups capable of forming covalent or van der Waals interactions with Si anodes.[4]

As reported earlier by several other research groups, polyacrylic acid (PAA) is employed in Si-based anodes in the linear polymeric form, in the neutralized form as NaPAA or LiPAA, cross linked with polyvinyl alcohol (PVA), CMC, *etc.* CMC is one of the most widely used commercial binders in Li-ion cells. The presence of hydroxy groups makes it a potential candidate for crosslinking with carboxylic acid containing polymeric binders like PAA.[4,5] Blending of Si with graphite (Gr) to form a Si–Gr composite along with carbon as an additive is reported by various groups. Graphite reduces the stress on the electrode coating by providing a porous structure that accommodates the volume change of Si, mitigates electronic contact losses and decreases SEI formation. LiPAA has been demonstrated as a promising binder for both Si–Gr anodes and for Ni-rich cathodes.[6] Table S1 summarises the reported studies on different binder systems for Si/Si–Gr anodes and the corresponding matrices employed. Heat treatment of Si–Gr and the carbon mixture reportedly improves the initial coulombic efficiency and charge retention. Also, heat treatment can increase inner pores and channels in spherical natural graphite.[7,8]

Crosslinking of binders is an effective strategy for improving the performance of Si–Gr composite anodes. In this context, cross-linked Tamarind Gum (TG)–PAA,[9] crosslinked dextrin,[10] a water-soluble binder of oxidized starch (OS) cross-linked with sodium carboxymethyl cellulose (OS–CMC),[11] glycol chitosan (GC) and lithium polyacrylate (LiPAA)[12] were reported by different research groups.

The present study attempts to understand the effectiveness of a crosslinked CMC–PAA binder on a thermally treated Si–Gr composite which is supported in graphite. Generally, the composition of Si based composite anodes has a conducting agent along with a binder. Here, in the present study, the Si–Gr composite is supported in a graphite matrix along with a conducting agent, a conductive binder (poly(3,4-ethylenedioxythiophene) and polystyrene sulfonate (PEDOT:PSS)) and a crosslinked binder (CMC–PAA). Apart from being electrochemically active, dispersing the Si–Gr composite in a graphite matrix (Si–Gr@Gr) is expected to relieve the stress developed in the electrode during expansion by acting as a mechanical buffer.[13–15] Heat treatment of the active material can modify the particle size, morphology, interplanar distance and particle-to-particle interaction which can positively influence the electrochemical performance.[16] In this attempt to understand the impact of the multipronged approach towards improving the performance of Si–Gr anodes, Fourier Transform Infrared Spectroscopy (FTIR) was employed to comprehend the behaviour of graphite, Si–Gr and Si–Gr@Gr active material powders and cross-linking of CMC and PAA. The powders were also characterised using X-ray Photoelectron Spectroscopy (XPS), X-ray Diffraction (XRD) and Field Emission Scanning Electron Microscopy (FESEM) analysis. Apart from mechanical integrity studies using FESEM and peel strength measurement, the Si–Gr@Gr anodes were electrochemically characterised in half cell configuration with Li metal as a counter electrode for understanding the cycling behaviour, rate capability, diffusion coefficient and impedance. The Si–Gr@Gr anode with the crosslinked CMC–PAA binder exhibited a specific capacity of 940 mA h g^{-1} with a coulombic efficiency of 80.3% and demonstrated 1000 charge–discharge cycles with 78% charge retention.

2. Experimental

2.1. Materials

Sodium CMC, Na-CMC (from M/s Nippon Paper Industries Co., Ltd) and PAA of average $M_v \sim 1\,250\,000$ (from M/s Sigma Aldrich) were used directly without further modification. Si–Gr composite powder with a Si mass fraction of 50 wt% and spherical graphite were purchased from M/s BTR Energy Materials. The other components of the electrode slurry include acetylene black (grade: Y50A, source: M/s SN2A, France) and poly(3,4-ethylenedioxythiophene):polystyrene sulfonate (PEDOT:PSS) (from M/s Sigma Aldrich) which is a conductive binder. PP/PE/PP trilayer polymer separator, Celgard 2320 from M/s Celgard, USA, was used as a separator. 1 M $LiPF_6$ in 1 : 1 (by weight) of ethylene carbonate : dimethyl carbonate (EC : DMC) with 2% fluoroethylene carbonate (FEC) as an additive was used as electrolyte.

2.2. Preparation of the CMC–PAA binder

The CMC–PAA binder solution was prepared by adding PAA powder step by step in deionised water with continuous stirring, until the mixture was homogeneous. Then, an equal quantity of CMC powder was added to it at once under continuous stirring on a magnetic stirrer for 3 h at 50 °C to obtain a CMC–PAA blend.

2.3. Preparation of the Si–Gr@Gr composites

The Si–Gr@Gr composite was prepared by the thermal annealing process, wherein a 1 : 1 weight ratio of Si–Gr powder and spherical graphite were mixed thoroughly in a mortar for 30 minutes for homogenization. The homogenised mixture was then transferred onto a quartz boat. The boat with the mixture was heated to 800 °C in a tube furnace at a ramp rate of 1 °C min^{-1} and kept at this temperature for 2 h to obtain the Si–Gr@Gr composite.

2.4. Preparation of the Si–Gr@Gr electrode

The Si–Gr@Gr composite was used as the active material of the electrode. The working electrode was fabricated by taking the components in the following weight ratio: 80 wt% of Si–Gr@Gr, 5 wt% of acetylene black, 5 wt% of CMC, 5 wt% of PAA and 5 wt% of conductive binder, PEDOT:PSS. At first, the Si–Gr@Gr composite was dry mixed with 5 wt% of acetylene black in a ball mill at 300 rpm for 30 minutes. The binder solution (CMC–PAA prepared earlier by dissolving in deionized water) was added to

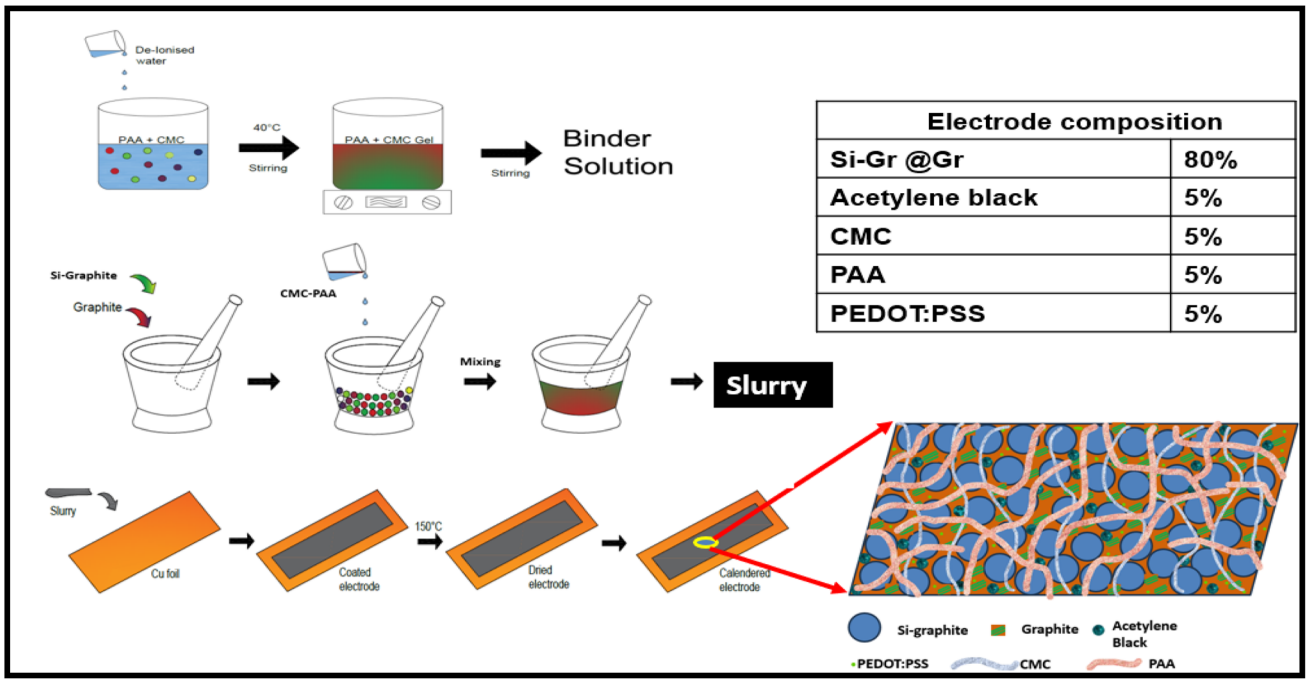

Electrode composition	
Si-Gr @Gr	80%
Acetylene black	5%
CMC	5%
PAA	5%
PEDOT:PSS	5%

Fig. 1 Preparation of a Si–Gr@Gr anode.

Table 1 Degree of substitution and viscosity of different grades of CMC

Grade	Degree of substitution (DS)	Viscosity (mPa s)
CMC (A)	0.85–0.95	1000–2500
CMC (B)	0.78–0.88	3000–5000
CMC (C)	0.65–0.75	6000–10 000

the dry mixed powder followed by adding 5 wt% of PEDOT:PSS. Ball milling was continued for another 30 minutes to get a homogeneous slurry. The obtained slurry was coated on copper foil of thickness 10 μm by using a doctor blade, and the as-prepared electrode was dried at 150 °C for 2 h under vacuum to completely remove residual water in the electrode and to facilitate esterification between CMC and PAA binders. At 150 °C, a condensation reaction occurs between the free carboxylic acid groups of PAA and the hydroxy groups of CMC, which afford interchain crosslinking. The preparation of the Si–Gr@Gr anode is depicted in Fig. 1. The electrode sheet was cut into a 12 mm diameter disk and used for the cell assembly. The active material loading of the Si–Gr@Gr active material on the electrode was ~0.8 mg cm^{-2}. The electrode thus prepared was assembled in a CR2032 coin cell using a PP/PE/PP trilayer polymer separator and 1 M $LiPF_6$ in EC : DMC (1 : 1) with 2% FEC electrolyte.

2.5. Material characterisation

FTIR studies were conducted using an M/s Thermo Fisher Scientific, model: iS50. An Instron-made peel tester was used for determining the peel strength of the electrode. XPS studies were done on a PHI 5000 Versa Probe II, ULVAC-PHI Inc., USA, while XRD was carried out on a Bruker D8 Discover. The viscosity of the binder mixtures was logged using a Brookfield Viscometer RV DV-1 Prime at 30 rpm. Electrochemical impedance spectra were recorded using an electrochemical workstation from M/s Ivium, the Netherlands (Model MP5).

2.6. Electrochemical measurements

The electrochemical performance tests of the coin cell were performed using an Arbin battery cycler in the galvanostatic mode, limiting discharge and charge potentials to 0.005 V and 3.0 V respectively, by using metallic Li as a counter electrode ("discharge" here refers to lithiation of the Si anode). The cells were charged and discharged at a C-rate of C/10 (1C = 1.12 mA) for the formation cycle and for the subsequent cycles. The capacity retention values were calculated with respect to the first discharge capacity obtained. All electrochemical measurements were carried out at 20 °C. Cyclic voltammetric studies were conducted on an Arbin cycling system (model no.: Arbin BT 2000).

3. Results and discussion

3.1. FTIR studies

3.1.1. Studies on PAA, CMC and CMC–PAA. Three different grades of CMC, labelled as A, B, C, with varying degrees of substitution (DS) were mixed with PAA in a 1 : 1 proportion and viscosity was measured. The mixture was coated on a polyethylene terephthalate (PET) support and dried at 150 °C in a vacuum oven for 17 hours to obtain binder films. The films

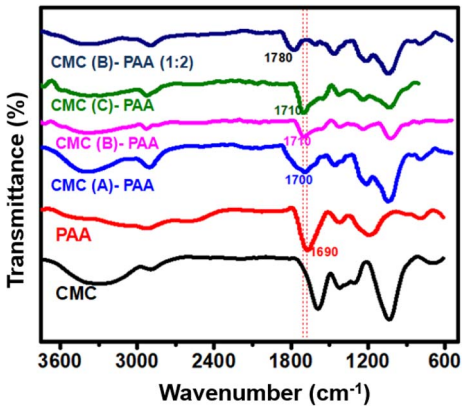

Fig. 2 FTIR spectra of CMC, PAA and CMC–PAA with different grades of CMC and proportions.

were subjected to FTIR characterisation. FTIR was recorded for the binder film with a 1 : 2 proportion of CMC : PAA also. The viscosity of the samples was measured before drying. The DS of the different grades and the viscosity of the binder mixture are tabulated in Table 1.

FTIR studies (Fig. 2) indicate the formation of ester bonds between the hydroxyl groups of CMC (B) and CMC (C) with the carboxylic acid groups of PAA. CMC (A) with the highest DS did not form ester bonds as fewer hydroxyl groups are available to react with the carboxylic acid groups of PAA. The viscosity of binder solutions increased with the decrease of DS of CMC, making it less favourable for slurry processing. Hence, CMC (B) which crosslinks with PAA with favourable viscosity was chosen as the grade of CMC for crosslinking with PAA. Crosslinking was also attempted by altering the proportion of CMC (B) : PAA to 1 : 2. A higher proportion of PAA in the mixture tends to form an anhydride as evidenced from the FTIR peak at 1780 cm^{-1}. Hence, the ratio of CMC : PAA was fixed at 1 : 1.

The typical FTIR spectra of CMC show peaks corresponding to C–O–C (1000–1150 cm^{-1}), CH_2 stretching (1400 cm^{-1}, 1550 cm^{-1}), C=O stretching (1600 cm^{-1}), CH stretching (2920 cm^{-1}), and OH stretching (3400 cm^{-1}). The FTIR spectra of PAA show an OH stretching peak at 3400 cm^{-1}, a CH_2 stretching peak at 1446 cm^{-1} and a C=O stretching peak of the carboxylic acid group at 1690 cm^{-1}. After drying, the peak corresponding to the carbonyl group has shifted to 1710 cm^{-1} in the case of both CMC (B) and CMC (C) which confirms the formation of ester bonds. The mechanism for the formation of ester bonds is given in Fig. 3.

3.1.2. Studies on active material powders. FTIR was recorded for graphite, Si–Gr powder and Si–Gr@Gr before and after heat treatment at 800 °C and is given in Fig. 4(a)–(c). Apart from the C–H stretching peak at 1440–1480 cm^{-1} in graphite and Si–Gr@Gr powders, the peaks at ~3400 cm^{-1}, 1640 cm^{-1}, 1000–1200 cm^{-1}, and 500–950 cm^{-1} corresponding to OH groups of Si–Gr/Gr, C=C, Si–O–Si/C–O–C and Si–O/C–O, respectively, are common in spectra of all samples. Post heat treatment, the intensity of all peaks decreased due to the removal of moisture and breakage of Si–O–Si/Si–O/C–O–C bonds. Upon heat treatment of Si–Gr@Gr, only the peaks at 3400 cm^{-1} and 1640 cm^{-1} get reduced while those in the 500–950 cm^{-1} region increase marginally. This could be attributed either to the formation of oxide on Si or to the interaction of the powders at high temperatures.

3.2. XPS studies

Fig. 5(a) and (b) show the XPS survey spectrum of Si–Gr@Gr before and after heating at 800 °C. From Fig. 6(a), the Si 2p XPS of Si–Gr powder before thermal treatment shows peaks at 100.5

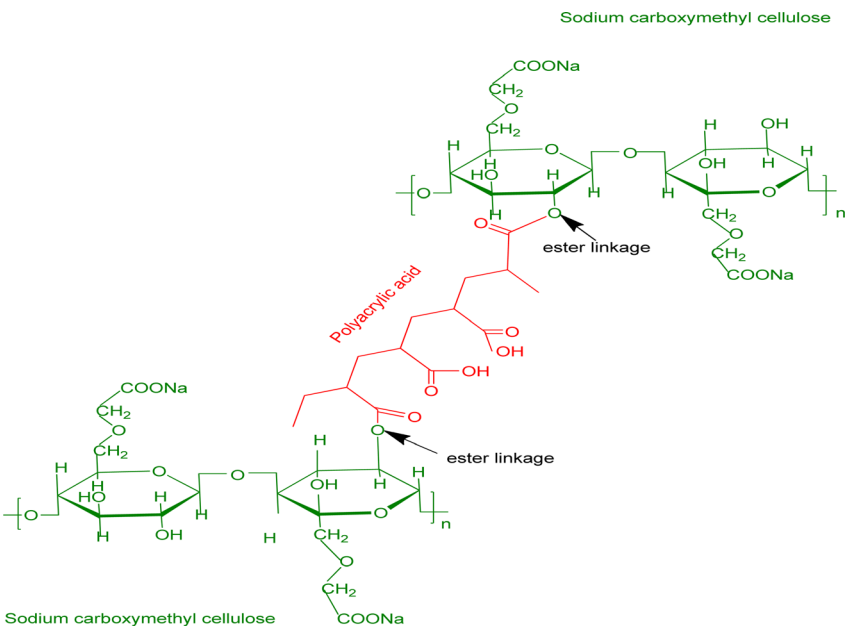

Fig. 3 Formation of ester bonds between CMC and PAA.

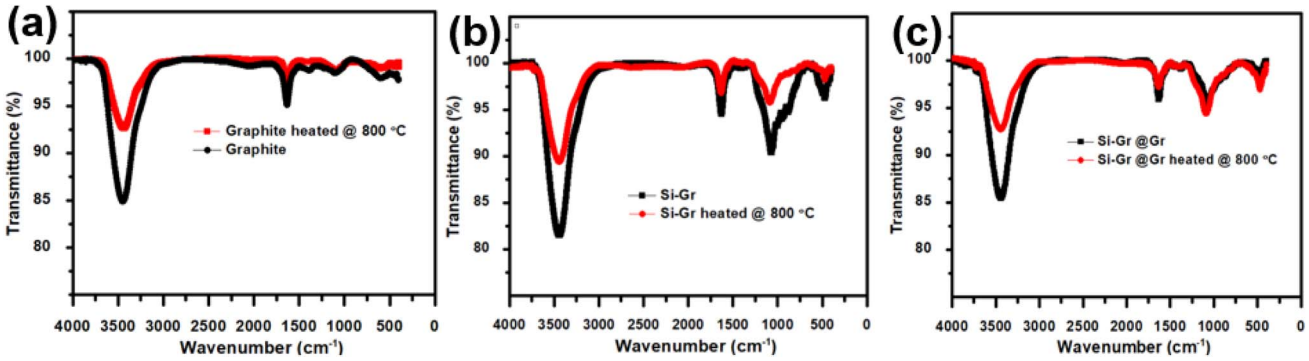

Fig. 4 FTIR spectra of (a) graphite, (b) Si–Gr and (c) Si–Gr@Gr before and after heating at 800 °C.

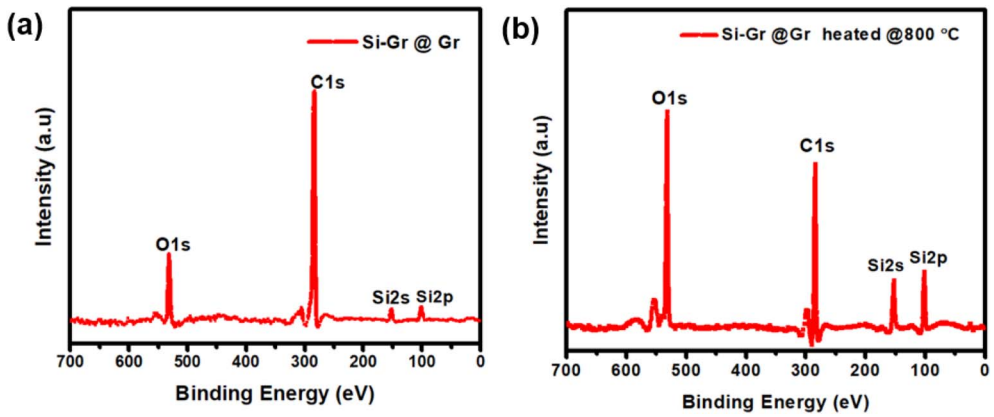

Fig. 5 XPS survey spectrum of Si–Gr@Gr powder (a) before heat treatment and (b) after heat treatment.

eV and 102.5 eV which correspond to Si–Si and suboxides of Si.[17,18] After thermal treatment (Fig. 6(b)) at 800 °C, the Si peak at 100.5 eV disappears and a peak at 103.5 eV appears. The new peak corresponds to SiO_2 which could have formed by the oxidation of Si upon heat treatment in air. The increase in intensity of the peaks post heat treatment indicates Si with an increased thickness of the SiO_x layer.[19] Two O 1s peaks, as seen in Fig. 6(c), located at 531 eV and 532.5 eV corresponding to C=O and Si–O, were detected in samples before heat treatment.[20] Upon heat treatment, the peak at 532.5 eV becomes sharper with a newly appeared minor peak at 530.5 eV (C–O) and a significant peak at 533 eV (C–O–Si/C–O–C) as seen in Fig. 6(d). The increase in intensity points to the oxidation upon heating and possible interaction between the particles of the powders. This observation is in agreement with the FTIR results for the active material powders. In Fig. 6(e) and (f), the C 1s peaks of Si–C, C–C and C–OH are detected at 283.7 eV, 284.8 eV and 285.6 eV, respectively, in the virgin material, in which peaks representing the oxidation of the active material appear after heat treatment, *viz.* 289 eV.[20–22]

3.3. Microstructure of active material powders

FESEM images of all active material powders were recorded before and after thermal treatment and are depicted in Fig. 7. Thermal treatment, in general, has changed the morphology and particle shape and size of the active material powders. Fig. 7(a) and (c) show the surface texture of graphite particles at 5k× and 25k×. The surface of the particle appears to be flaky, but very closely packed. But after heat treatment, the surface appears to be broken with all the flakes loosely packed as evident from Fig. 7(b) and (d). This provides additional pathways for free movement of Li-ions in the matrix. A similar observation is noted on the surface and particle size of Si–Gr@Gr powder also under identical magnification (before heating – Fig. 7(e) and (f) and post heating – Fig. 7(g) and (h)). After heat treatment, the Si–Gr particles appear to be smaller (Fig. 7(i) and (j)).

3.4. X-ray diffraction studies of active material powders

The XRD patterns of graphite, Si–Gr and Si–Gr@Gr are shown in Fig. 8(a)–(c), respectively. The 2θ values and d-spacing are provided in the inset of each figure. The XRD pattern of pristine graphite shows characteristic peaks of graphite at 26.501°, 42.306° and 54.550° with d-values of 3.3607 Å, 2.13464 Å and 1.68092 Å, respectively which are indicative of the highly ordered carbon structure of graphite.[25] The peaks could be well matched with the diffraction pattern of the graphite with *hkl* values of [002], [100], [101] and [004] (PDF 00-008-0415). Upon thermal treatment, the 2θ values decrease to 25.254°, 40.094° and 54.361° with a corresponding increase in the d-values

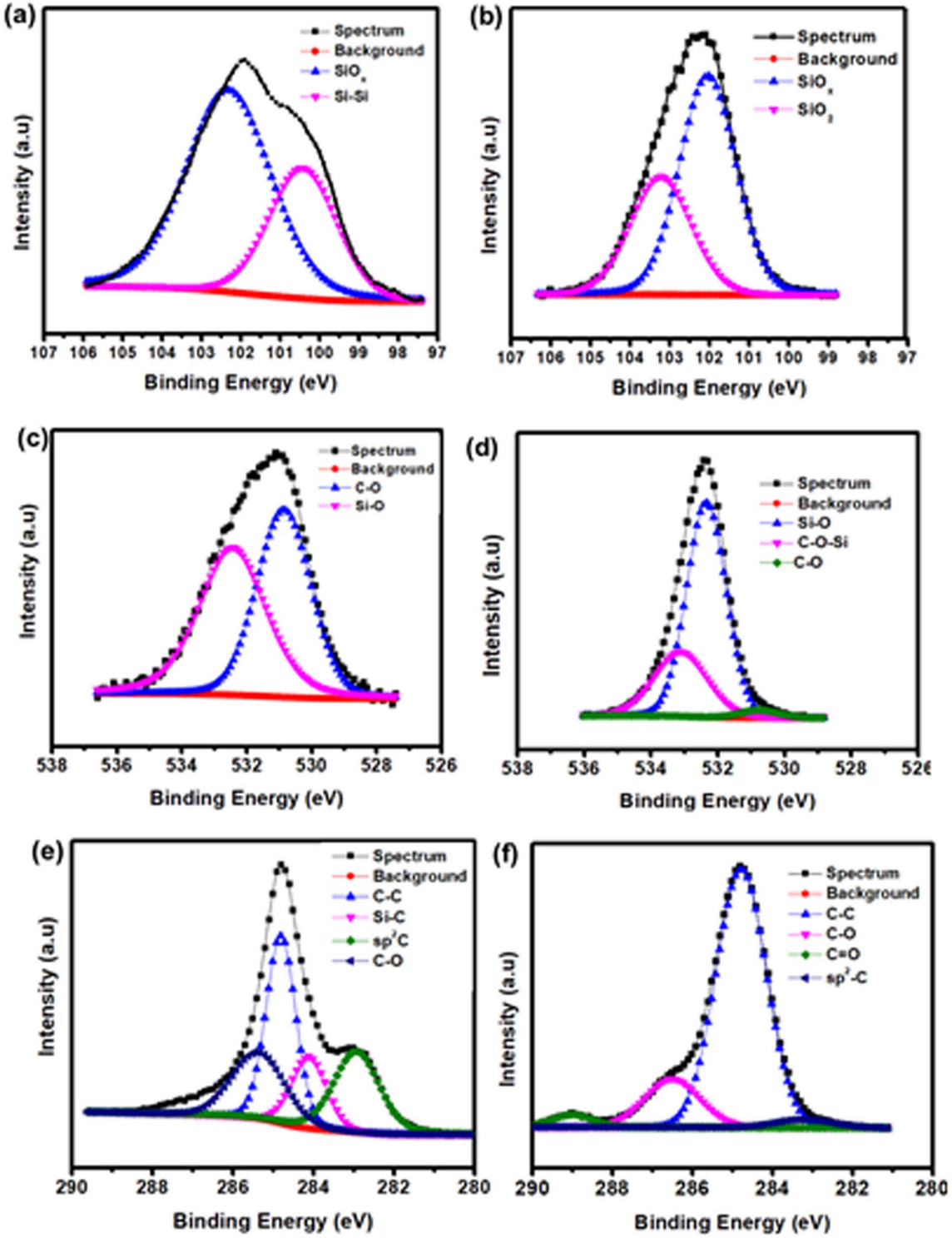

Fig. 6 Si 2p XPS peaks of Si–Gr@Gr powder (a) before heat treatment and (b) after heat treatment. O 1s XPS peaks of Si–Gr@Gr powder (c) before heat treatment and (d) after heat treatment. C 1s XPS peaks of Si–Gr@Gr powder (e) before heat treatment and (f) after heat treatment.

(Fig. 8(a)). This increase in the interlayer distance can be attributed to the intercalation of oxygen during thermal treatment in air (Fig. 9). Though there is a change in *d*-values, graphite maintains its graphitic nature despite oxidation.[23] Morphology of the particles also indicates the flakier nature of the material post thermal treatment. Similar observations are made from the XRD patterns of pristine Si–Gr and Si–Gr after heat treatment (Fig. 8(b)). The XRD patterns of the procured Si–Gr composite show a peak at 28.4° corresponding to Si and strong peaks in the 2θ ranges of 20–30°, 45–50° and 55° corresponding to graphite. The peaks at 28°, 47°, 55°, 69° and 76° correspond to diffraction planes [111], [220], [311], [400] and

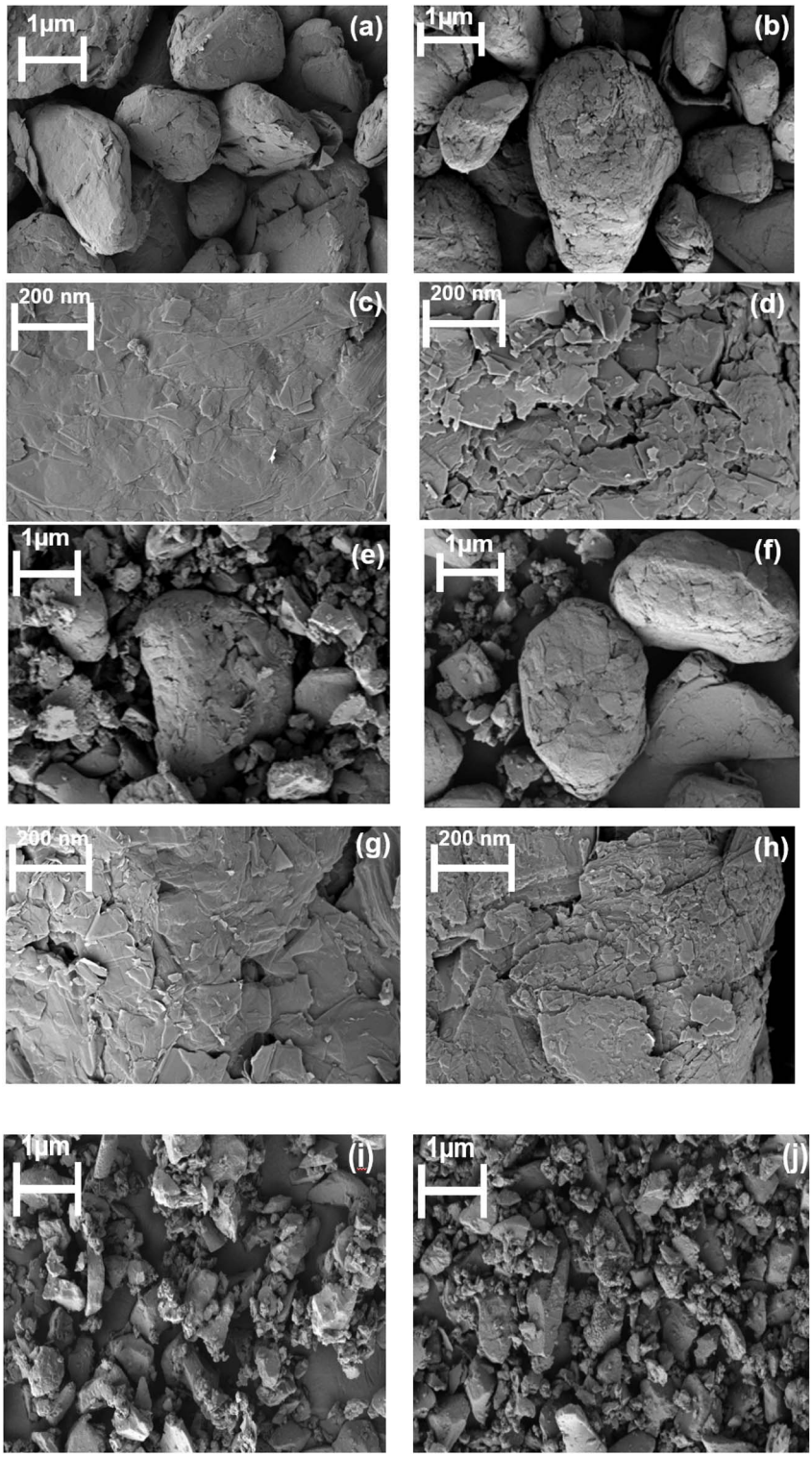

Fig. 7 FESEM of Gr (a) and (c) before and (b) and (d) after heat treatment, Si–Gr@Gr (e) and (g) before and (f) and (h) after heat treatment and Si–Gr (i) before and (j) after heat treatment (magnification of (a), (b), (e), (f), (i) and (j) is 5k× while (c), (d), (g) and (h) are at a magnification of 25k×).

[331] respectively which perfectly match that of Si (PDF 01-077-2107). The weak intensity of the Si diffraction peaks in the composite is possibly due to the low content of Si in the composite.[24] Similar to graphite, the 2θ peaks shifted to lower values and the corresponding d-values increased which could be attributed to the oxidation of the powder. The XRD patterns of the Si–Gr@Gr composite show peaks at 26.5° and 54.7°, corresponding to graphite and 28.4° corresponding to Si. The

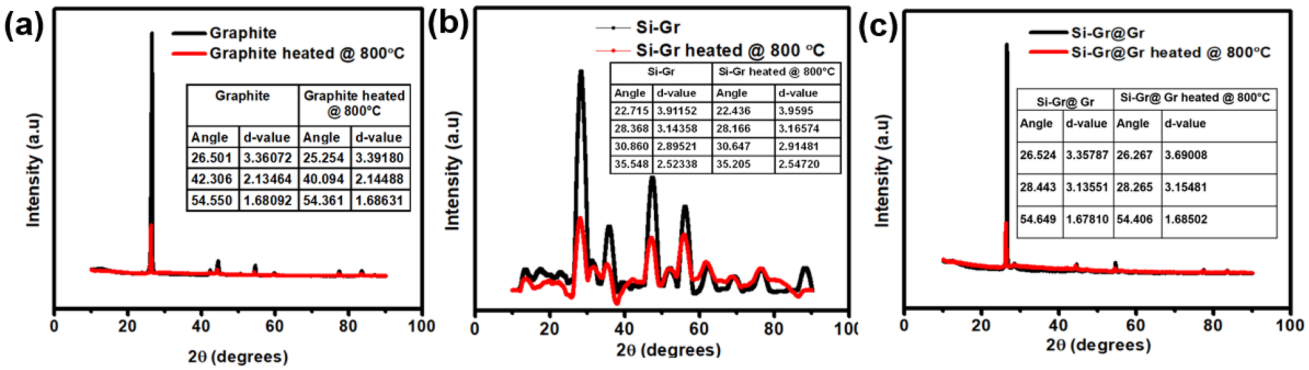

Fig. 8 XRD pattern of (a) graphite, (b) Si–Gr and (c) Si–Gr@Gr before and after heat treatment.

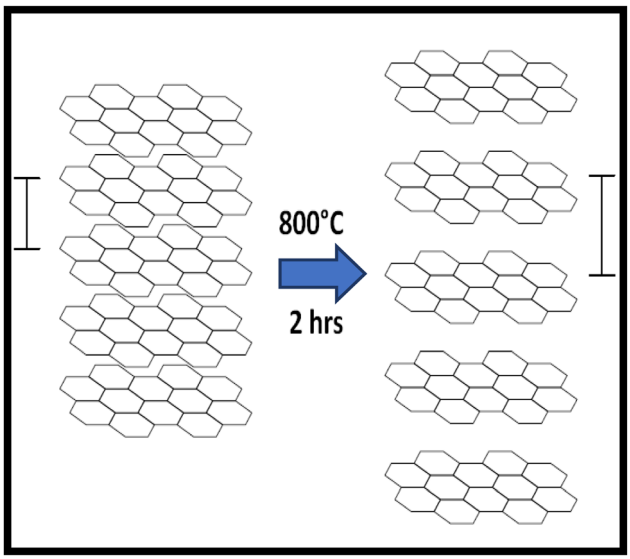

Fig. 9 Schematic of change in interplanar spacing of the active material upon thermal treatment.

crystallite size of Si–Gr@Gr decreased from 57.6 nm to 39.3 nm upon thermal treatment. All peaks and the *d*-values decreased upon thermal treatment due to oxidation of the particles (Fig. 8(c)). This is supported by the XPS patterns of Si–Gr@Gr which indicates the oxidation of the particles. The FTIR and XPS results support the formation of oxides. Also, morphological changes noted from the FESEM images of the powder before and after thermal treatment contribute to the variation in XRD peaks. This matches with the FTIR, XPS and morphological changes noted in the FESEM images of the powder before and after thermal treatment. There is a decrease in intensity of XRD peaks which indicates that the amorphous nature of the sample has increased upon thermal treatment. XRD patterns of graphite and Si–Gr@Gr before and after heating are separately provided in Fig. S2–S5.

3.5. Electrode level characterisation

3.5.1. Peel strength. The peel strength of the electrode provides a measure of adhesion between the active material–conducting agent–binder composite and the copper current collector. It is equally important for the active material along with the binder to maintain cohesiveness to enable electrical continuity of the matrix. The peel strength of the Si–Gr@Gr electrode with the CMC–PAA binder was evaluated according to ASTM 903. The ability of the electrode to sustain the load during the test as a function of displacement/extension is depicted in Fig. 10. The corresponding peel strength of the Si–Gr@Gr electrode with the CMC–PAA binder is ~130 gf cm^{-1}. The adhesion force of the Si–Gr@Gr anode originates from the crosslinking of CMC and PAA. The adhesion test clearly indicates that the robust ester bonds between CMC and PAA contribute to the mechanical strength of the electrode. The impact of peel strength is evident from the microstructure of electrodes. The electrodes with good peel strength values could sustain the mechanical stress due to volume expansion of the active material without withering even after 1000 galvanostatic charge–discharge cycles.

3.5.2. Electrochemical characterisation. The electrolyte used in the present study was 1 M $LiPF_6$ in EC : DMC (1 : 1 by wt) with 2% FEC as an additive. This electrolyte was chosen for the study as FEC containing electrolyte formulations are reported to

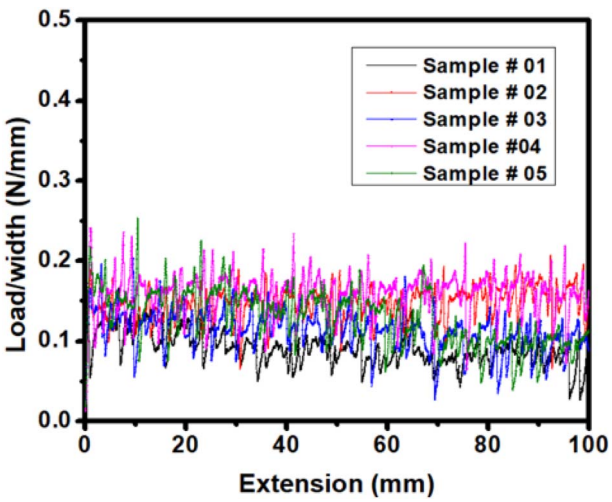

Fig. 10 Peel strength of the Si–Gr@Gr electrode.

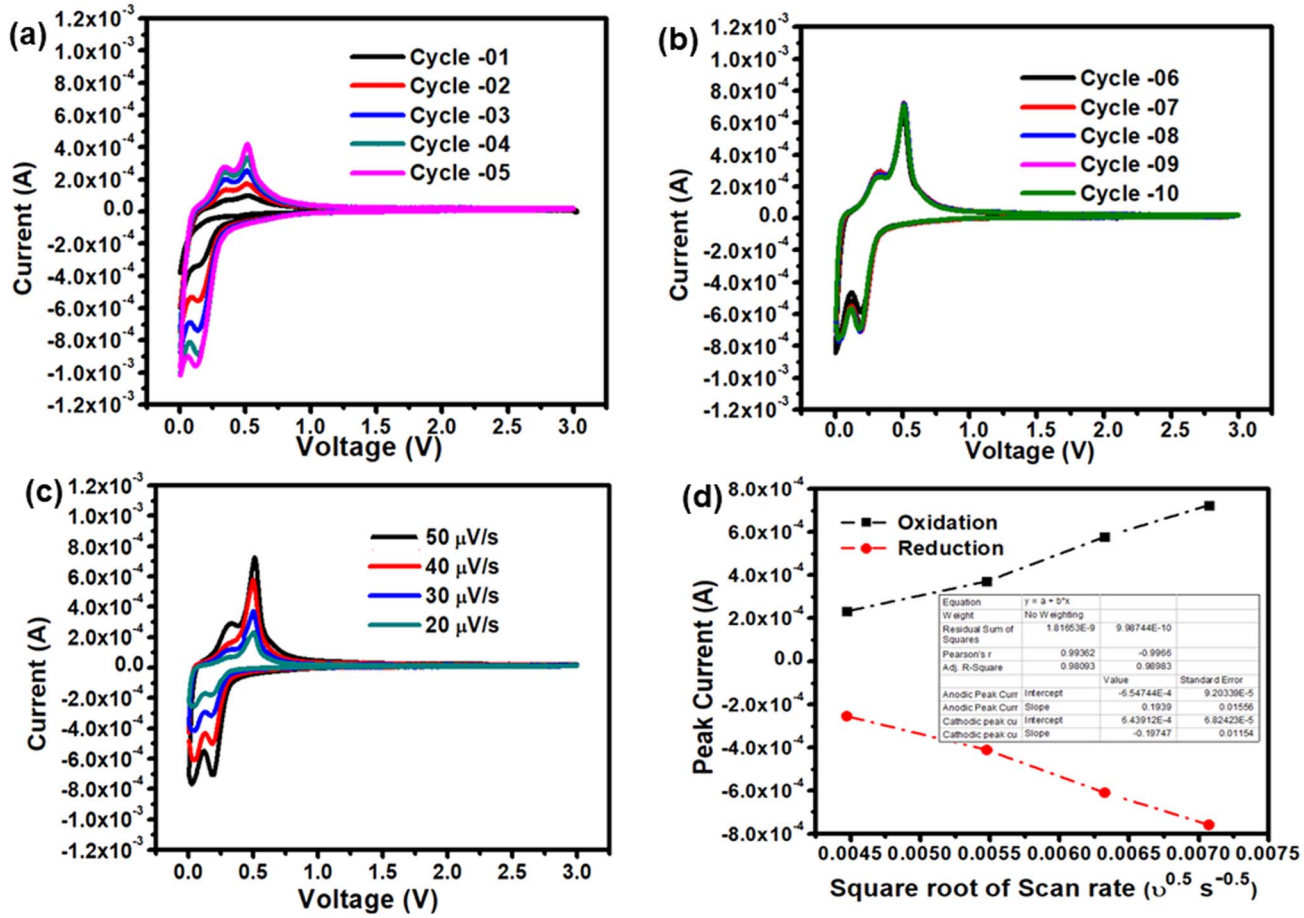

Fig. 11 (a) and (b) CV of the Si–Gr@Gr electrode from cycles 1 to 10, (c) CV of the Si–Gr@Gr electrode at different scan rates and (d) plot of peak current *vs.* square root of the scan rate.

have a positive effect in SEI stabilisation and help counter electrode volume changes by forming cross-linked polymers during the formation cycles by reductive decomposition.[13] The coin cells were initially scanned at 50 μV s^{-1} from OCV to 0.005 V and then back to 3 V for the first cycle and then the potential window was fixed between 0.005 V and 3 V for the subsequent cycles. It can be seen that the current increases upon cycling and attains a steady value. Upon scanning cathodically, the Si–Gr@Gr electrode with the crosslinked CMC–PAA binder displays two strong peaks, at ~0.18–0.20 V and ~0.05 V. The former corresponds to the formation of Li–Si amorphous phases while the latter is due to the phase transition from amorphous Li_xSi to crystalline $Li_{15}Si_4$. The anodic peaks at ~0.35 V and ~0.5 V are attributed to the de-alloying process from lithiated Si to Si. As reported earlier, due to the progressive activation of the active material, a gradual increase in the intensity of the anodic and cathodic peaks is noted.[25] Also, the SEI film on the electrode is not completely formed in the first cycle. Upon electrochemical cycling, stable SEI film formation happens due to which the cathodic current and anodic current tend to stabilize in the subsequent scans, as shown in Fig. 11(a) and (b). This is also reflected in the efficiency of the cell during galvanostatic charge–discharge cycling. The first cycle efficiency was ~80% which gradually increased to 100% upon cycling.

After completing five formation cycles at 50 μV s^{-1}, cyclic voltammetric scans at different scan rates *viz.* 40 μV s^{-1} followed by 50 μV s^{-1}, 30 μV s^{-1} and 20 μV s^{-1} were conducted. Upon increasing the scan rates, a corresponding increase in peak current was also noted (Fig. 11(c)). For the peaks, apart from being sharp and well-defined, the positions are identical at every scan rate, signifying the good cyclability of the Si–Gr@Gr anode with the crosslinked CMC–PAA binder.[25] This observation is supported by the galvanostatic charge–discharge performance of the cell. Furthermore, it could be elucidated that a linear relationship exists between the cathodic and anodic peak current (i_p) and the square root of the scanning rates used (Fig. 11(d)). This data were used to calculate the Li-ion diffusion coefficient for both the oxidation (de-lithiation) and reduction (lithiation) processes in the Si–Gr@Gr anode with the crosslinked CMC–PAA binder, using the classical Randles–Sevcik equation

$$i_p = (2.69 \times 10^5) n^{3/2} A D_{Li^+}{}^{1/2} C^*_{Li} v^{1/2}$$

where i_p, n, D_{Li^+}, A, C^*_{Li} and v denote the peak current, number of electrons transferred, diffusion coefficient, concentration and scan rate, respectively. The diffusion coefficients obtained for the cathodic and anodic reactions are 3.88 × 10^{-9} cm^2 s^{-1} and 3.74 × 10^{-9} cm^2 s^{-1}, respectively, which are in reasonable

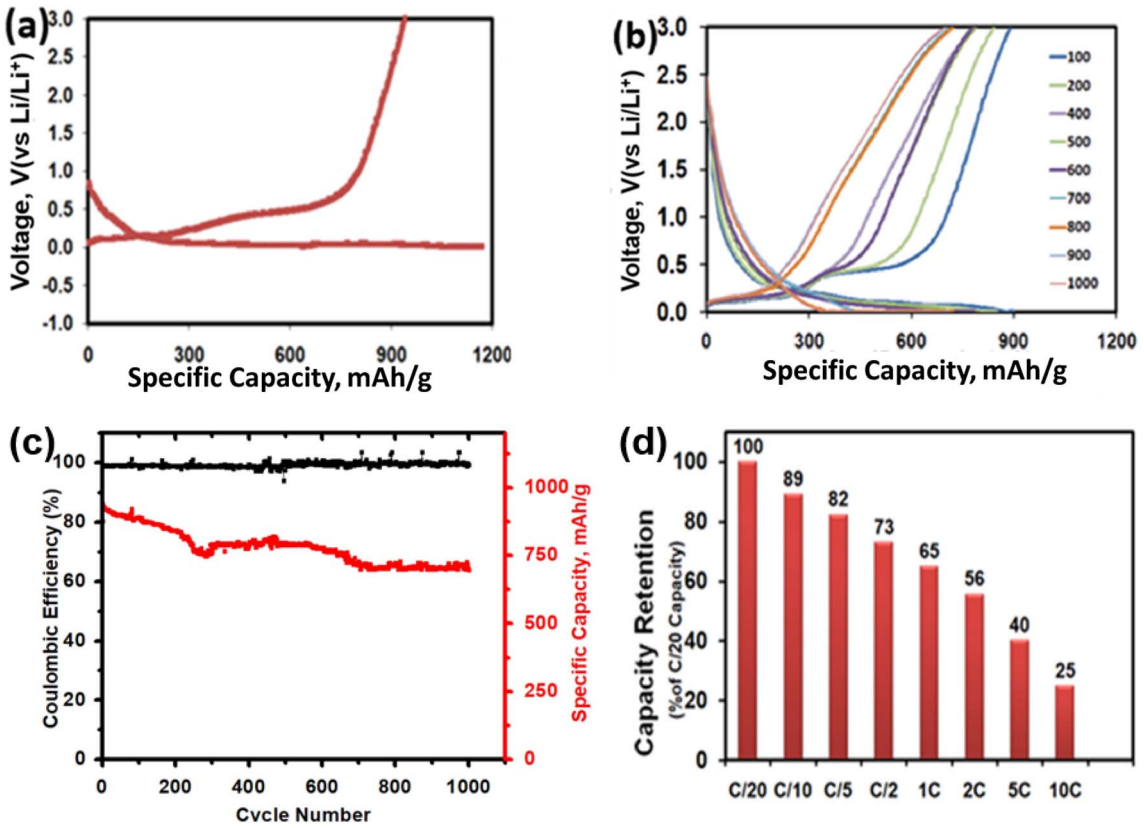

Fig. 12 (a) First cycle charge–discharge characteristics at a C/10 rate, (b) charge–discharge characteristics for different cycles at a C/10 rate, (c) variation in specific capacity and coulombic efficiency upon continuous cycling at a C/10 rate and (d) rate capability studies of the Si–Gr@Gr electrode.

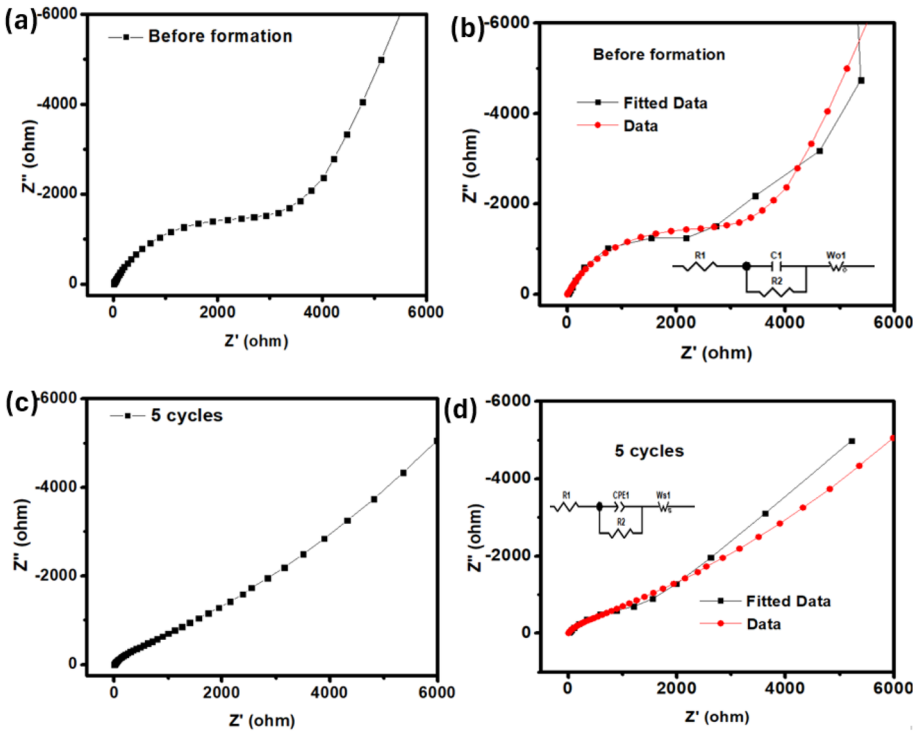

Fig. 13 EIS spectra of the Si–Gr@Gr anode with the crosslinked CMC–PAA binder (a) before formation, (b) fitted data before formation, (c) after 5 cycles and (d) fitted data after 5 cycles.

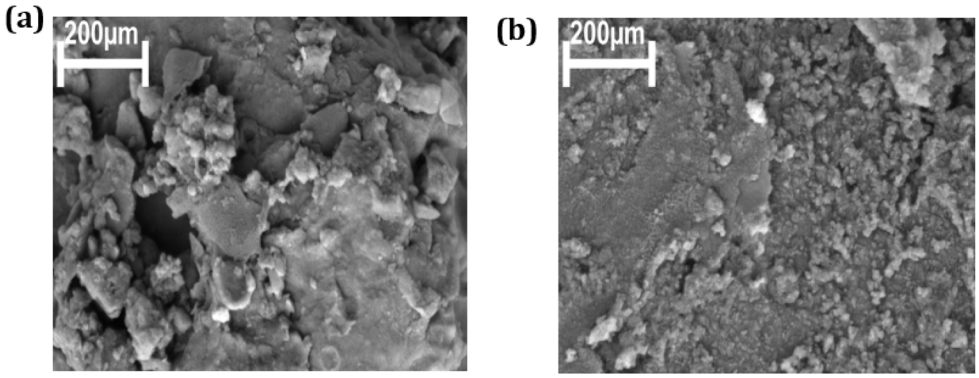

Fig. 14 FESEM images of the Si–Gr@Gr electrode with the CMC–PAA binder (a) before cycling and (b) after 1000 cycles.

agreement with reported values.[26,27] Table S2 provides diffusion coefficients for graphite/Si/Si–Gr anodes reported on similar systems while Fig. S1 reproduces the error margins for anodic and cathodic peak current.

The Si–Gr@Gr anode with CMC–PAA as a binder with PEDOT:PSS as a conductive agent was evaluated against metallic lithium as a counter electrode in a CR2032 coin cell. The formation cycle of the half-cell was carried out at a C/10 rate. FEC is a proven additive which helps control the impedance growth resulting from the repeated formation and cracking of the SI layer due to volume expansion.[8,28] The cell exhibited an initial cycle specific capacity of 940 mA h g^{-1} with an efficiency of 80.3%. The first cycle charge–discharge performance is depicted in Fig. 12(a).

The cell was subjected to continuous galvanostatic charge–discharge tests at a C/10 rate. The cell has demonstrated 1000 cycles with a capacity retention of 78%.

The specific capacity recorded at the end of 1000 cycles is 730 mA h g^{-1}. The efficiency values were maintained at ~100%. The cycling performance at every 100th cycle, the capacity/efficiency variation with cycles and the performance at different rates are given in Fig. 12(b)–(d), respectively.

The Si–Gr@Gr anode-based cells were subjected to electrochemical impedance spectroscopy in the frequency range from 100 kHz to 0.01 Hz before formation (Fig. 13(a) and (b)) and after five cycles (Fig. 13(c) and (d)). The charge transfer resistance reduces significantly (~30%) after five cycles indicating the highly conductive nature of the matrix and the formation of a stable SEI layer.

3.5.3. Microstructure analysis of electrodes. FESEM images of Si–Gr@Gr electrodes with the CMC–PAA binder were recorded before cycling and after the completion of 1000 cycles. The microstructure of electrodes (Fig. 14(a) and (b)) reveals very close bonding between the particles which proves that the binder is highly effective in holding the particles together, as supported by the peel strength of the electrode. Post cycling microstructure analysis reveals that the electrode matrix is intact without any cracking due to the continuous expansion/contraction process associated with the lithiation and de-lithiation process. The particles maintain the connectivity, contributing to the overall integrity of the anode even after the completion of 1000 cycles. The strong adhesion to the substrate and the cohesive interaction among particles, imparted by the crosslinked CMC–PAA binder, enhanced the peel strength of the electrode and thereby improved its electrochemical performance. The crosslinked CMC–PAA binder has also provided the electrode the necessary elasticity to accommodate the volume expansion and maintain the integrity of the electrode. Heat treatment of the active materials and dispersion of the Si–Gr composite in graphite has also helped in alleviating the stress in the electrode by probably opening up the channels for the lithiation and de-lithiation process.

4. Conclusions

In summary, this study demonstrates the effectiveness of a multipronged approach to alleviate the performance degradation associated with volume expansion in Si–Gr anodes, by employing a facilely crosslinked CMC–PAA binder dispersed in an aqueous medium together with thermally treated Si–Gr powder supported on graphite. The robust crosslinked binder network, which is constructed through the esterification process, as confirmed by FTIR studies, has favourably assisted in stress dissipation due to volume expansion. The effect of thermal treatment on Si–Gr@Gr, which has positively contributed to improving the performance by buffering the mechanical stress, was systematically investigated by FTIR, XPS and XRD. The enhancement of mechanical integrity of the electrodes against volume expansion is also evidenced from the peel strength and FESEM microstructures. The EIS signatures and diffusion coefficients for the cathodic and anodic reactions obtained through CV support the efficacy of the approach adopted. The electrochemical evaluation of Si–Gr@Gr anodes with crosslinked CMC–PAA exhibited an initial coulombic efficiency of 80.3% and first cycle specific capacity of 940 mA h g^{-1}. A capacity retention of ~78% with a specific capacity of 730 mA h g^{-1} at the end of 1000 cycles is direct evidence of the beneficial impact of this multipronged approach on extended cycling. Therefore, this study provides a useful strategy for the rational design of crosslinked binders and devising process parameters to address the problem of severe volume changes associated

with such Si–Gr based anodes which is a major impediment to the commercialisation of Si–Gr based anodes.

Conflicts of interest

There are no conflicts to declare.

Data availability

The data supporting the findings of this study are available on request.

Supplementary information is available. See DOI: https://doi.org/10.1039/d5su00186b.

Acknowledgements

The authors would like to extend wholehearted thanks to Director, Vikram Sarabhai Space Centre (VSSC), for the support towards publishing this research paper.

References

1 R. Z. A. Manj, F. Zhang, W. U. Rehman, W. Luo and J. Yang, Toward understanding the interaction within silicon-based anodes for stable lithium storage, *Chem. Eng. J.*, 2020, **385**, 123821.
2 H. Ahmed, G. S. dos Reis, P. Molaiyan, A. Lähde and U. Lassi, Silicon/carbon composite anode materials for lithium-ion batteries: materials design and synthesis, current state, progress, and future perspectives, *Prog. Energy*, 2025, **7**(2), 022003.
3 X. Zhao, S. Niketic, C. H. Yim, J. Zhou, J. Wang and Y. Abu-Lebdeh, Revealing the Role of Poly(vinylidene fluoride) Binder in Si/Graphite Composite Anode for Li-Ion Batteries, *ACS Omega*, 2018, **3**, 11684–11690.
4 Y. Yang, S. Wu, Y. Zhang, C. Liu, X. Wei, D. Luo and Z. Lin, Towards efficient binders for silicon based lithium-ion battery anodes, *Chem. Eng. J.*, 2021, **406**, 126807.
5 N. Hamzelui, G. G. Eshetu and E. Figgemeier, Customizing Active Materials and Polymeric Binders: Stern Requirements to Realize Silicon-Graphite Anode Based Lithium-Ion Batteries, *J. Energy Storage*, 2021, **35**, 102098.
6 B. Boz, K. Fröhlich, L. Neidhart, P. Molaiyan, G. Bertoni, M. Ricci, F. De Boni, M. Vuksanovic, M. Romio, K. Whitmore and M. Jahn, Evaluating Polyacrylic Acid as a Universal Aqueous Binder for Ni-Rich Cathodes NMC811 and Si Anodes in Full Cell Lithium-Ion Batteries, *ChemPlusChem*, 2024, **89**, e202400195.
7 S. Zhu, Y. Lin, Z. Yan, J. Jiang, D. Yang and N. Du, Novel design of uniform Si@Graphite@C composite as high-performance Li-ion battery anodes, *Electrochim. Acta*, 2021, **377**, 138092.
8 L. Gehrlein, C. Njel, F. Jeschull and J. Maibach, From Additive to Cosolvent: How Fluoroethylene Carbonate Concentrations Influence Solid-Electrolyte Interphase Properties and Electrochemical Performance of Si/Gr Anodes, *ACS Appl. Energy Mater.*, 2022, **5**, 10710–10720.
9 A. Samridh, S. V. Gopinadh, B. John, S. Sarojiniamma, M. T. Devassia and M. G. Joseph, Sustainable Binder System: Cross-Linked Tamarind Gum-Polyacrylic Acid for Silicon-Graphite Anodes in Future Lithium-Ion Batteries, *Energy Technol.*, 2025, **13**(5), 2401837.
10 S. Chen, H. Y. Ling, H. Chen, S. Zhang, A. Du and C. Yan, Development of cross-linked dextrin as aqueous binders for silicon based anodes, *J. Power Sources*, 2020, **450**, 227671.
11 R. You, X. Han, Z. Zhang, L. Li, C. Li, W. Huang, J. Wang, J. Xu and S. Chen, An environmental friendly cross-linked polysaccharide binder for silicon anode in lithium-ion batteries, *Ionics*, 2019, **25**, 4109–4118.
12 P. F. Cao, M. Naguib, Z. Du, E. Stacy, B. Li, T. Hong, K. Xing, D. N. Voylov, J. Li, D. L. Wood III and A. P. Sokolov, Effect of binder architecture on the performance of silicon/graphite composite anodes for lithium ion batteries, *ACS Appl. Mater. Interfaces*, 2018, **10**(4), 3470–3478.
13 O. Naboka, C. H. Yim and Y. Abu-Lebdeh, Practical Approach to Enhance Compatibility in Silicon/Graphite Composites to Enable High-Capacity Li-Ion Battery Anodes, *ACS Omega*, 2021, **6**, 2644–2654.
14 S. He, S. Huang, S. Wang, I. Mizota, X. Liu and X. Hou, Considering Critical Factors of Silicon/Graphite Anode Materials for Practical High-Energy Lithium-Ion Battery Applications, *Energy Fuels*, 2021, **35**, 944–964.
15 L. Xu, J. Wang and C. Su, Preparation and electrochemical performances for silicon-carbon ternary anode materials with artificial graphite as conductive skeleton, *J. Solid State Electrochem.*, 2024, **28**, 2445–2454.
16 I. H. Sohel, T. Ozturk, U. Aydemir, N. S. Peighambardoust, O. Duygulu, I. Isık-Gulsac, M. Altun and M. N. Ates, Deciphering the effect of the heat treatment on the electrodeposited silicon anode for Li-ion batteries, *J. Energy Storage*, 2022, **55**, 105817.
17 F. Jeschull, F. Lindgren, M. J. Lacey, F. Bjorefors, K. Edstrom and D. Brandell, Influence of inactive electrode components on degradation phenomena in nano-Si electrodes for Li-ion batteries, *J. Power Sources*, 2016, **325**, 513–524.
18 R. Azmi, F. Lindgren, K. Stokes-Rodriguez, M. Buga, C. Ungureanu, T. Gouveia, I. Christensen, S. Pal, A. Vlad, A. Ladam, K. Edstrom and M. Hahlin, An XPS Study of Electrolytes for Li-Ion Batteries in Full Cell LNMO vs. Si/Graphite, *ACS Appl. Mater. Interfaces*, 2024, **16**, 34266–34280.
19 D. Yang, T. Lv, J. Song, J. Chen, L. Hao, Q. Tian and L. Cui, Enabling stable high lithium storage of Si anode via synergistic effects of nanosized Fe_3C and partially graphitized porous carbon, *Chem. Eng. J.*, 2024, **496**, 153844.
20 G. Zheng, Y. Xiang, L. Xu, H. Luo, B. Wang, Y. Liu, X. Han, W. Zhao, S. Chen, H. Chen, Q. Zhang, T. Zhu and Y. Yang, Controlling Surface Oxides in Si/C Nanocomposite Anodes for High-Performance Li-Ion Batteries, *Adv. Energy Mater.*, 2018, **8**, 1801718.
21 M. Furquan, M. K. Jangid, A. R. Khatribail, S. Vijayalakshmi, A. Mukhopadhyay and S. Mitra, Mechanical and Electrochemical Stability Improvement of SiC-Reinforced Silicon-Based Composite Anode for Li-Ion Batteries, *ACS Appl. Energy Mater.*, 2020, **3**, 12613–12626.

22 N. R. Tanguy, J. N'Diaye, M. Arjmand, K. Lian and N. Yan, Facile one-pot synthesis of water-dispersible phosphate functionalized reduced graphene oxide toward high-performance energy storage devices, *Chem. Commun.*, 2020, **56**, 1373–1376.
23 T. Zhang, J. Gao, L. J. Fu, L. C. Yang, Y. P. Wu and H. Q. Wu, Natural Graphite coated by Si nanoparticles as anode materials for lithium ion batteries, *J. Mater. Chem.*, 2007, **17**, 1321–1325.
24 C. Xiao, P. He, J. Ren, M. Yue, Y. Huang and X. He, Walnut-structure Si-G/C materials with high coulombic efficiency for long-life lithium ion batteries, *RSC Adv.*, 2018, **8**, 27580–27586.
25 E. Barcaro, V. Marangon, M. Mutarelli and J. Hassoun, A lithium-ion battery with cycling stability promoted by the progressive activation of a silicon oxide anode in graphene-amorphous carbon matrix, *J. Power Sources*, 2024, **595**, 234059.
26 J. Kang, K. Rah, S. Lee and S. M. Park, Kinetics on Li Deintercalation in Mg- or Li-Doped SiO/Graphite Composite Anodes for Li Ion Batteries: Dopant Effect, *J. Phys. Chem. C*, 2023, **127**, 20255–20266.
27 S. H. Nguyen, J. C. Lim and J. K. Lee, Electrochemical characteristics of bundle-type silicon nanorods as an anode material for lithium ion batteries, *Electrochim. Acta*, 2012, **74**, 53–58.
28 S. Yamazaki, R. Tatara, H. Mizuta, K. Kawano, S. Yasuno and S. Komaba, Consumption of Fluoroethylene Carbonate Electrolyte-Additive at the Si-Graphite Negative Electrode in Li and Li-Ion Cells, *J. Phys. Chem. C*, 2023, **127**, 14030–14040.